Open Research Online

The Open University's repository of research publications
and other research outputs

Modelling of an imaging beamline at the ISIS pulsed neutron source

Journal Item

How to cite:

Burca, G.; Kockelmann, W.; James, J. A. and Fitzpatrick, M. E. (2013). Modelling of an imaging beamline at the ISIS pulsed neutron source. Journal of Instrumentation, 8(10), article no. P10001.

For guidance on citations see FAQs.

© 2013 IOP Publishing

Version: Accepted Manuscript

Link(s) to article on publisher's website:
http://dx.doi.org/doi:10.1088/1748-0221/8/10/P10001

Copyright and Moral Rights for the articles on this site are retained by the individual authors and/or other copyright owners. For more information on Open Research Online's data policy on reuse of materials please consult the policies page.

oro.open.ac.uk

PUBLISHED BY IOP PUBLISHING FOR SISSA MEDIALAB

RECEIVED: *July 3, 2013*
ACCEPTED: *August 25, 2013*
PUBLISHED: *???, 2013*

Modelling of an imaging beamline at the ISIS pulsed neutron source

G. Burca,[a,b,1] **W. Kockelmann,**[b] **J.A. James**[a] **and M.E. Fitzpatrick**[a]

[a]*Materials Engineering, The Open University, Milton Keynes, MK7 6AA, U.K.*
[b]*STFC, Rutherford Appleton Laboratory, ISIS Facility, Chilton, OX11 0QX, U.K.*

E-mail: genoveva.burca@stfc.ac.uk

ABSTRACT: A combined neutron imaging and neutron diffraction facility, IMAT, is currently being built at the pulsed neutron spallation source ISIS in the U.K. A supermirror neutron guide is required to combine imaging and diffraction modes at the sample position in order to obtain suitable time of flight resolutions for energy selective imaging and diffraction experiments. IMAT will make use of a straight neutron guide and we consider here the optimization of the supermirror guide dimensions and characterisation of the resulting beam characteristics, including the homogeneity of the flux distribution in space and energy and the average and peak neutron fluxes. These investigations take into account some main design criteria: to maximise the neutron flux, to minimise geometrical artefacts in the open beam image at the sample position and to obtain a good energy resolution whilst retaining a large neutron bandwidth. All of these are desirable beam characteristics for the proposed imaging and diffraction analysis modes of IMAT.

KEYWORDS: Instrumentation for neutron sources; Inspection with neutrons; Neutron radiography; Beam-line instrumentation (beam position and profile monitors; beam-intensity monitors; bunch length monitors)

[1]Corresponding author.

© 2013 IOP Publishing Ltd and Sissa Medialab srl

doi:xxxxxxx

proofs JINST_003P_0713

Contents

proofs JINST_003P_0713

1 Introduction

Neutron imaging facilities serve numerous users and research projects worldwide, whether they are under operation at research reactors or continuous spallation sources. Currently no neutron imaging instruments exist at pulsed neutron sources, which would enable them to take advantage of the timing structure of the neutron beam, but several such instruments are in the design or construction stage, for example IMAT at ISIS, U.K. [1], VENUS at the SNS Oak Ridge, U.S.A. [2] and ERNIS at J-PARC, Japan [3]. IMAT will be a thermal and cold neutron facility for imaging and diffraction applications which will be built on the ISIS second target station (TS-2) at the Rutherford Appleton Laboratory, U.K. TS-2 is a low-power pulsed spallation source of approximately 50 kW operated at 10 Hz.

A neutron imaging system includes three main components: a neutron source, a collimator system and a detector. A collimation system is required to form the moderated neutrons into a useful neutron beam in order to reduce the propagation direction of the radiation and to obtain a well-defined image of the sample. Many of the existing neutron radiography facilities use a pinhole geometry for neutron beam collimation. Because IMAT will combine imaging and diffraction techniques on one beamline, a possibility which is not currently available at any other single instrument, it will also have a neutron guide for obtaining a good time resolution for diffraction measurements as well as energy-selective imaging whilst retaining a good neutron flux. The use of a neutron guide is unusual for an imaging instrument, and the neutron optics need to be optimized in order to maximize the neutron flux and to minimise the geometrical artefacts which may be seen in the open

beam image at the sample position, see for example [4]. From the initial performance requirements as dictated by the science case [1] it is recognised that the incident energy spectrum and timing resolution requirements for both the imaging and diffraction modes are similar, which is an imperative condition for a combined instrument on the same moderator of a neutron source. Another important aspect favourable for a dual-use beamline is that IMAT will be able to be switched from imaging to diffraction mode by simply moving the aperture selector to an open position and adjusting the beam jaws to the desired gauge volume. The combination of diffraction and imaging on one beamline will enable more advanced studies on materials than possible if separate beamlines were used. By taking advantage of the Bragg edges in the energy-dependant neutron cross-section and by exploiting the capability of a pulsed source to select optimal energies, materials which are not visible with the standard neutron radiography can be made visible or transparent. Hence, while microstructure properties (e.g. crystallographic texture) can be mapped with high resolution in transmission mode, the diffraction data will be required to determine the complete orientation distribution function. IMAT will be set-up for in-situ studies and processing, for example texture measurements in combination with strain measurements at non-ambient conditions (e.g. at elevated temperatures or under load), in-situ sintering or welding. The concurrent acquisition of transmission and diffraction data to study irreversible processes will be a major advantage of the instrument. The approach will allow investigations of samples by imaging followed by a detailed diffraction analysis of the regions of interest by selecting any point within the 2D or 3D sample [5, 6]. By adding sample geometry acquired through imaging data, the diffraction scans benefit in terms of positioning accuracy, in order to obtain more focussed information about the stress state or the material's composition at a particular point which often cannot be obtained by diffraction alone.

This paper presents results from Monte Carlo ray-tracing simulations [7] as applied to the IMAT instrument operating in imaging mode. In particular the effect of the straight, square neutron guide on the intensity and wavelength distribution of the beam and hence on the quality of the neutron radiography is investigated.

It should be noted that curved and elliptical neutron guides were tested for IMAT. The curved neutron guide produces an asymmetric image on the monitor due to Garland reflections [8]. The elliptical guide produces a large divergence which is unfavourable for strain scanning diffraction measurements compared to the straight guide.

Of particular relevance for an instrument built on a pulsed source and with a neutron guide is the characterisation of spatial and spectral intensity distributions, flux values, beam divergence and homogeneity of the beam profile. The characterization of the beam allows the performance of IMAT for both white beam imaging and wavelength-dependent imaging to be estimated.

Standard white-beam tomography integrates the attenuation coefficients over all energies of the spectrum and hence many wavelength dependent features are lost in the averaged data. Energy-selective measurements however allow the possibility of selecting narrow wavelength bands so that the energy-dependent attenuation effects are visible. Various mechanisms are in use for performing energy selective measurements at other facilities, including the turbine device at continuous sources [9] or reflection by single crystals based on a double-crystal monochromator [10] or the slit method, which uses more than two single crystals to reject neutrons which are outside of the wavelength band required [11]. At ISIS, which is a pulsed source, the energies are selected via time-of-flight measurements (TOF) [12]. Using this method the neutron wavelength (and hence

proofs JINST_003P_0713

the corresponding energy) can be determined from the distance it has travelled to the detector position (l) and the travel time (t) taken to do so, i.e. $\lambda = \frac{ht}{ml}$. The TOF method has the advantage that each pulse contains the full thermalized neutron spectrum and so a large number of Bragg edges [13] can be observed in a single measurement.

2 Modelling of the neutron imaging beam for IMAT

2.1 General layout

The main components of IMAT are: a neutron source and moderator, a supermirror neutron guide, choppers for defining the wavelength band, a pinhole selector, sets of slits for shaping the beam, a sample positioning system and imaging and diffraction detectors. Many parameters of the IMAT instrument stem from the source parameters of the ISIS TS-2 [14] which is a short-pulse source, operated at 10 Hz, and equipped with cold moderators designed to produce long wavelength neutrons. One of five proton pulses produced by the ISIS synchrotron is directed onto the TS-2 tungsten target. Both the imaging and diffraction applications of the IMAT instrument benefit from the highest possible neutron flux and this can be achieved using a coupled moderator filled with liquid hydrogen (20 K) and solid methane (26 K) at the back of the hydrogen container. The positioning of the instrument on such a moderator is at the expense of producing a relatively broad pulse, and as a consequence, a somewhat reduced energy resolution.

The flight path of 56 m, from the centre of the moderator to the sample position, ensures good time-of-flight and energy resolution while preserving a large neutron wavelength bandwidth. Three choppers will be placed into gaps in the neutron guide: a T0 chopper serving as a fast neutron and gamma radiation filter and two double disk-choppers defining the wavelength band required to prevent the frame-overlap of neutrons between successive neutron pulses. The pair of double-disk choppers can operate in a number of modes, for example, a 'single-frame' operation with a bandwidth of about 6 Å at the source frequency of 10 Hz and a frame length of 0.1 s, or a 'double-frame' operation with a bandwidth of about 12 Å with the double-disk chopper running at 5 Hz repressing every second neutron pulse, and with a time frame of 0.2 s between successive pulses.

The bandwidths are derived from the frame lengths, 0.1 s and 0.2 s respectively, taking into the account the finite opening times of the choppers yielding 0.7–6.8 Å and 1.4–13.6 Å for the single and double operations, respectively. Moreover, the wavelength bands can be shifted by changing the chopper phase offsets (i.e. the time offset of the chopper opening with respect to the neutron generation at t-zero). IMAT is not limited to operations with broad bandwidths. By changing the phases of the choppers, narrow wavelength bands, down to widths of 0.5 Å, can be selected to pass to the sample position. However, IMAT will usually be operated with a broad wavelength band and with imaging cameras able to discriminate wavelengths by the time-of-flight method. By triggering the camera with the ISIS 't-zero' pulse of the neutron generation, images can be collected as a function of time-of-flight.

The achievable wavelength resolution is determined by the capabilities of the camera system but ultimately limited by the widths of the neutron pulses generated in the target-moderator system. Figure 1a, b show the pulse width (ΔT) as well as the energy resolution (ΔT/T) at 56 m, i.e. at the position of the IMAT imaging detector. For a 700 μ s long-wavelength pulse width at about 6 Å

proofs JINST_003P_0713

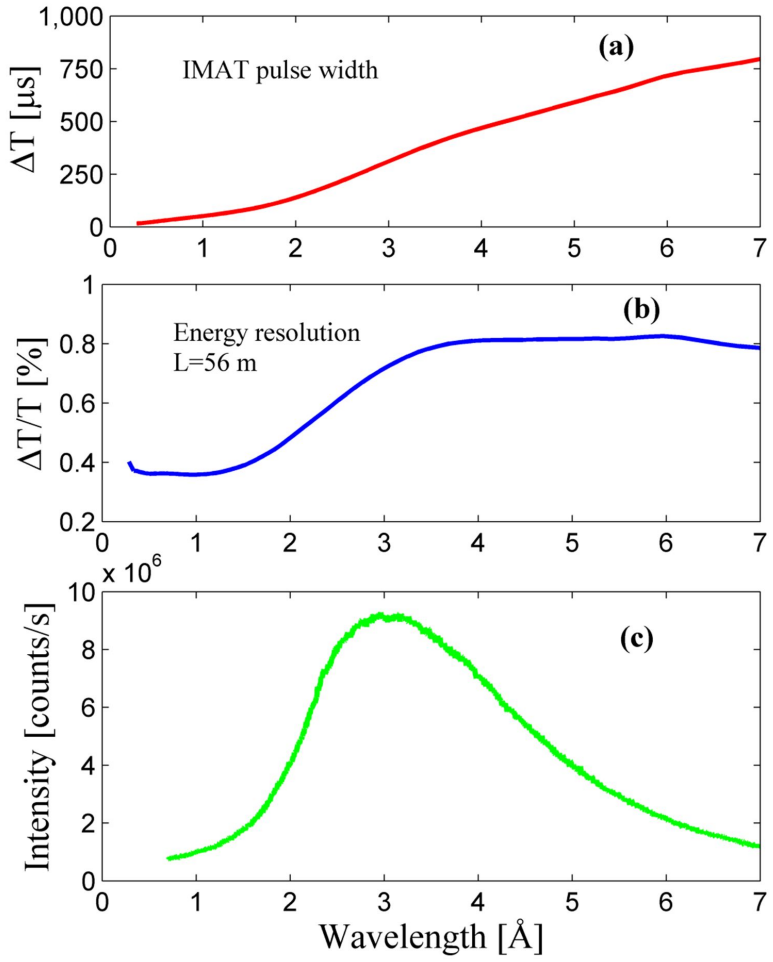

Figure 1. Moderator pulse width (ΔT) (a) resolution (ΔT/T) as function of wavelength (b), IMAT spectrum given by the lambda monitor placed on the sample position for wavelength band 0.7–7 Å with maximum at 3 Å (c).

a worst resolution of $\Delta T/T \sim 0.8\%$ is obtained; the wavelength resolution is better at higher and lower wavelength. The thermalised IMAT flux has a maximum at around $3\mathring{A}$ (figure 1c) and the maximum 'single-frame' wavelength value (at the end of the 0.1 s time period between two successive neutron pulses) is about $7\mathring{A}$ for 56 m, slightly larger than twice the value of peak-wavelength, which makes the IMAT wavelength band convenient for efficient collection, i.e. peak wavelengths are not heavily over-counted and long wavelengths are not under-counted.

In imaging mode IMAT will use a beam emanating from a pinhole. A variable circular pinhole aperture with five opening diameters D=5, 10, 20, 40 and 80 mm, placed at the guide exit yields collimation ratios of L/D=2000, 1000, 500, 250, 125 for a given flight path from the pinhole to the detector of L=10 m. Both imaging and diffraction modes will make use of beamline slits, which will be used to control the divergence of the beam or to restrict the size of the beam, for example in imaging mode to illuminate only part of a sample or the active area of the camera. In theory,

proofs JINST_003P_0713

two sets of slits are sufficient to collimate a beam. However, although the edges of the jaws will mostly absorb neutrons, they will also partially scatter or transmit them. To catch these neutrons as effectively as possible, IMAT will have additional sets of slits.

A sample manipulation system will be available to position a sample in the neutron beam and to rotate a sample for the collection of projections for tomographic reconstruction. Samples will be analysed in a single acquisition if the sample is smaller than the sensitive area of the neutron camera, or in a scanning mode if the sample is bigger than the camera area.

The imaging cameras of IMAT will use the TS-2 source trigger signal to determine neutron wavelengths by the time-of-flight (TOF) method. A gated CCD camera system based on a flat scintillator screen [15] will collect projections for a given wavelength band by specifying a TOF offset and TOF window. A system with high temporal resolution and capable of measuring multiple wavelength bands in a single frame is envisaged to fully exploit the pulsed source for optimum energy discrimination and efficient data collection schemes. Such a system, e.g. based on microchannel plates [16], will enable pixel-by-pixel total cross section measurements and Bragg edge transmission analysis [17]. The maximal beam size at the sample position is determined by the distance (L) of the camera downstream from the pinhole and by the divergence of the neutron beam after the pinhole. For IMAT the distance 'L' was chosen to be 10 m, yielding a beam diameter of approximately 20 cm. Diffraction detector arrays at different 2θ scattering angles, with a total coverage of 4 steradians, will be installed for diffraction analysis. Every array is composed of individual scintillation detector elements (pixels) each having a rectangular size of $4\times100\,\mathrm{mm}^2$. The main IMAT instrument parameters are given in table 1.

With the set of beamline jaws and one set of slits placed just in front of the sample the beam size at the sample position can be adjusted from $200\times200\,\mathrm{mm}^2$ for imaging to typically $1\times1\,\mathrm{mm}^2$ for diffraction applications. The switching from imaging to diffraction experiments will be made by modifying the pinhole size to the open beam position and adjusting the jaws to give the desired beam size on the sample position.

2.2 Modelling approach

The Monte-Carlo modelling package McStas 1.12c [7] was used to model and optimize various aspects of the IMAT instrument design. McStas is based on a Meta Language and is designed for modelling neutron scattering instruments. The software package permits parallel computing, i.e. each simulation can be processed by a varying number of CPUs for decreasing the computation time, e.g. with the GridMP platform provided by ISIS [18, 19]. The Grid works in two basic modes, parameter scan mode (where a batch of smaller jobs are executed on a distributed machine) and in large scan mode (where one single job with e.g. 10^{10} neutrons, is broken into smaller chunks which are executed in parallel across many machines). For either mode, results are merged post-computation. In general, for a good representation of the performance of an instrument at least a few million neutron trajectories are calculated because then the statistical uncertainty is lower than 1% [7, 20]. In our simulations we've used 10^{10} neutrons and the statistical error confirms the previous statement, being around 1% or lower for neutron flux values. For a detailed review of the McStas statistical errors of calculations we encourage the readers to consult McStas references mentioned above.

proofs JINST_003P_0713

Table 1. Main IMAT instrument parameters.

General:	
Moderator	L-H2 / S-CH4 (W5 port on TS-2)
Repetition rate	10 Hz
Neutron guide	m=3, straight, square $100\times100\,mm^2$ in 2 m long shutter section $95\times95\,mm^2$ for ~42 m guide
Choppers	T0 (20 Hz), 2 double-disk choppers (10 Hz)
Single/double frame bandwidth	0.68 - 6.8 Å / 1.36–13.6 Å
Flight path to sample	56 m
Imaging:	
L: Distance pinhole — sample D: Aperture diameter	10 m 5, 10, 20, 40, 80 mm
L/D	2000, 1000, 500, 250, 125
Best spatial resolution	50 μm
Max Field of View	$200\times200\,mm^2$
Detector types	Gated CCD camera using ZnS/LiF or gadox scintillators TOF pixel detector (based on A. Tremsin — MCP detector specification [16]) with Timepix readout
Diffraction:	
Secondary flight path	2.0 m (at $2\theta = 90$ degree)
Detector type	ZnS/LiF scintillator with wavelength-shifting fibre readout; detector arrays at $2\theta = 20, 45, 90, 125, 155$ degrees
Angular detector coverage	4 steradians (1 steradian at 90 degrees)
Gauge sizes	1, 2, 5, 10 mm

Our preliminary McStas model comprised a basic imaging instrument making use of the following McStas components: ISIS moderator, neutron guide, pinhole and monitor (figure 2). The given dimensions and positions were: area of the moderator face $11\times11\,cm^2$, moderator-guide entrance distance of 1.7 m (the closest possible distance to a moderator on TS-2), an adjustable circular pinhole aperture situated at 1.5 m downstream from the guide exit, a flight path from the pinhole to the monitor position of 10 m. The m-value of the neutron guide is 3.

A number of monitor and detector components are available for users in McStas. Here only three types of monitors were utilised: the PSD (position sensitive detector, which acts like a beam monitor) to investigate the spatial distribution of the neutron intensity, a wavelength sensitive 'lambda monitor' and a divergence/wavelength monitor modified for the present imaging performance calculations. The imaging camera on IMAT will be capable of taking on the roles of the McStas PSD and lambda-monitors, however with a much increased number of pixels of about 1000×1000 whereas the McStas monitors used for the present simulations have 100×100 pixels on a $20\times20\,cm^2$ screen. The number of wavelength bins in the simulations was typically 1000.

proofs JINST_003P_0713

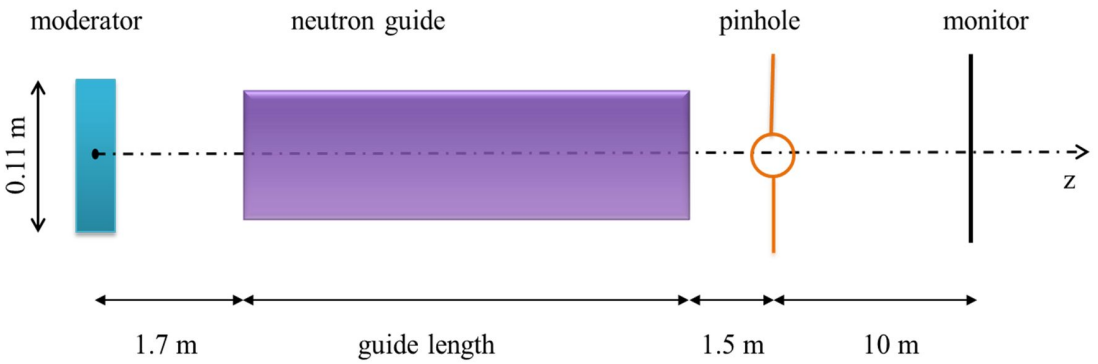

Figure 2. Sketch of the instrument components and geometry corresponding to the preliminary McStas model. The guide starts at 1.7 m from the moderator and the pinhole is positioned at 1.5 m from the guide exit. At the sample position (at 10 m from the pinhole) a PSD is placed which substitutes for the imaging detector. The neutron propagation is in the direction of the z-axis. The PSD is in the xy-plane.

The 'ISIS moderator' component employed in the McStas simulations was developed by the ISIS TS-2 Target Development Team [21] using the MCNPX MonteCarlo package [22]. The wavelength dependence of the pulse width of the composite hydrogen/methane moderator, shown in figure 1a, is a result of MCNPX calculations. The use of the simulated ISIS moderator component in McStas gives the largest contribution to the systematic uncertainties in our calculations. Based on experimental data and simulations from existing instruments on TS2 built on the same hydrogen/methane moderator we expect the IMAT parameters to be within a factor of 2 of McStas simulated pulse widths and time-integrated neutron fluxes. The McStas IMAT model described above assumes a number of simplifications. For example the real neutron guide for the IMAT instrument consists of several sections with gaps for choppers, diagnostic monitors and vacuum valves (the largest gap is 335 mm for T0 chopper and the smallest gap between guide sections is 2 mm). In this preliminary stage of modelling the gaps in the neutron guide were neglected. A continuous, straight guide of square cross section was modelled. Typically, 10^{10} neutrons were generated in a wavelength band of 0.1–10 Å. All calculations during this study have been performed without considering the effect of gravity on the neutron trajectories.

2.3 Spatial distribution of intensities for white beam imaging

As mentioned above, the imaging mode of the IMAT will use a pinhole from which a beam will emanate to form a neutron imaging beam of about $20\times20\,\mathrm{cm}^2$ at the sample position. The spatial distributions of neutrons on the monitor placed on the sample position in the case of the white beam measurements reveal vertical and horizontal stripes. Here we aim to characterize the stripes, to illustrate their origin and to see how they could be minimalized or removed.

2.3.1 Artefacts investigations

The simulated imaging data, based on the model presented in figure 2, show vertical and horizontal stripes (hereafter, 'artefacts') in the form of intensity dips in the neutron intensity distribution at the

proofs JINST_003P_0713

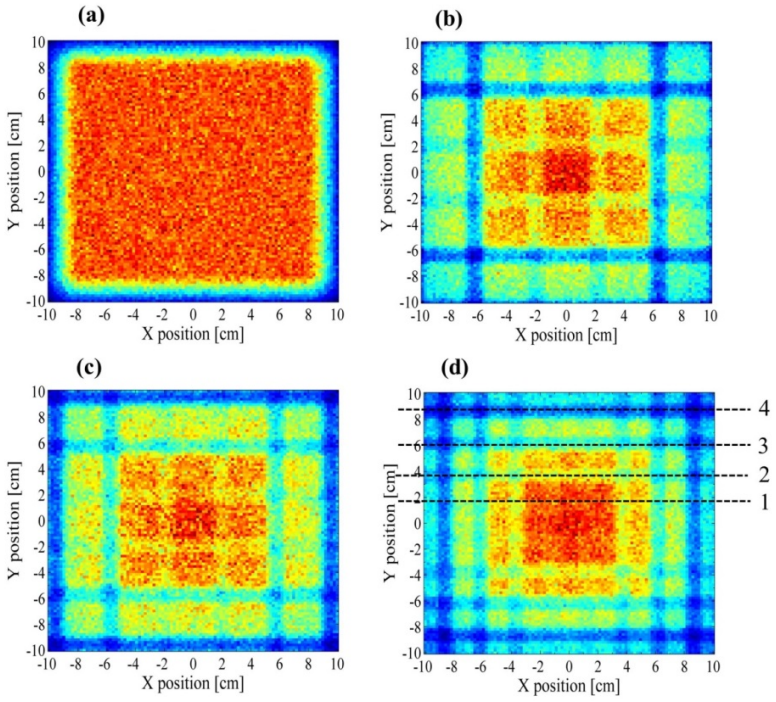

Figure 3. Neutron intensity distributions at the monitor position for an aperture diameter of 10 mm and for different m=3 guide lengths (a) 2.8 m; (b) 23.8 m; (c) 26.8 m; (d) 42.8 m. The number and depths of the artefacts are increasing as the guide length increases. The guide cross section is the same as the moderator size (11×11 cm^2).

monitor position. These artefacts are shown in figure 3 for different lengths of the neutron guide, indicating the geometrical origin of these stripes. Such artefacts have been observed before (e.g. [4]) and were explained by inadequacies of the transport system with regard to under-illumination of the guide entry, misalignment of guide sections, and gaps in the guide. Here we present a simple geometrical model which allows detailed exploration of the origin and characteristics of these artefacts. Initially, four different guide lengths with the same cross section as the moderator (i.e. 11×11 cm^2) were modelled.

It was noticed that the artefacts increased in number depending on the neutron guide length. For a very short guide, e.g. 2.8 m, one stripe is visible at the edge of the monitor (figure 3a). Increasing the guide length up to 42.8 m increases the number of artefacts (figure 3d).

A simple ray-tracing approach was applied to a two-dimensional pinhole camera model of the guide-pinhole system as shown in figure 4. This ray-tracing module developed in C++ [23] allows, in addition to the McStas simulations, to elucidate geometrical effects of the moderator-guide-pinhole-detector system in a rapid and quantitative manner in two dimensions. It should be noted that the ray-tracing code assumes 100% reflectivity of the neutron guide.

Selecting rays emanating from points with different vertical positions on the monitor (from point B up to point A) with a step of 0.01 and tracking their path back up to moderator, their origins (here, the distance EF on the moderator) were calculated [23] based on an infinitesimally small pinhole diameter.

proofs JINST_003P_0713

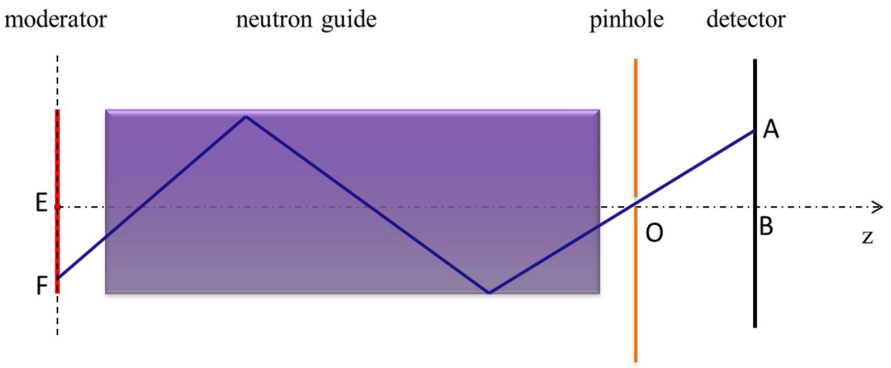

Figure 4. Outline of a basic instrument model to elucidate positions and widths of artefacts. The blue line represents the neutron path traced backwards from point A on the monitor to point F on the moderator. The red line represents the moderator face with height of 0.11 m.

Figure 5 shows that there are positions on the detector (values of AB) for which the position of corresponding rays, when traced back to the position of the moderator, lie outside of the moderator, i.e. these points can receive no neutrons and correspond to the gaps in intensity detected by the PSD (figure 3). Due to the symmetry of the image the stripes were calculated only on the half upper part of the monitor (the positive y-axis values). The ray-tracing approach was further extended by adding a finite pinhole size instead of the infinitesimal one. Hence, the finite pinhole size was modeled by numerically integrating over the pinhole (i.e. summing images generated using infinitely small pinholes across the actual pinhole diameter). Figure 6 compares profile plots of the intensity distributions from the McStas simulation obtained by normalizing the average neutron intensity across the PSD from figure 3 (i.e. summing all rows and dividing by the maximum value), its Gaussian fitting profile and the ray-tracing calculation for a pinhole with diameter of 10 mm and a guide length of 42.8 m. The positions of the artefacts produced on the PSD by McStas using the 42.8 m guide and a pinhole diameter of 10 mm (figure 3d) do agree well with the positions predicted by the ray-tracing code shown in figure 5.

Table 2 lists the parameters obtained by fitting Gaussian functions to the intensity dips (position, height, FWHM, area) for two different pinholes, D=5 mm and D=10 mm. The artefacts as observed on the PSD output have a finite depth, with the shallower artefacts in the monitor's centre and the more pronounced artefacts at the edge of the monitor. It should be emphasized that the artefacts for the finite pinhole sizes are not completely devoid of neutrons, whereas the ray-tracing model with infinitely small pinhole does produce blind spots as indicated in figure 5.

The widths of the artefacts as approximated by the full width at half maximum (FWHM) for each McStas peak of the profile are different from the widths (w) (figure 5) as determined from the ray-tracing for the infinitely small pinhole. For the latter, the widths decrease from 0.3 cm to 0 when moving from the edge of the screen to the centre. The widths from McStas simulations are generally larger and of the order of the size of the pinhole. This indicates that for finite pinholes the widths of artefacts are dominated by the pinhole size (washing out effect) (figure 6). For the smaller pinhole size of 5 mm, a decrease of the width towards the centre of the screen as predicted by the ray-tracing is observed. Both ray-tracing and McStas predict artefacts of varying depth (height),

proofs JINST_003P_0713

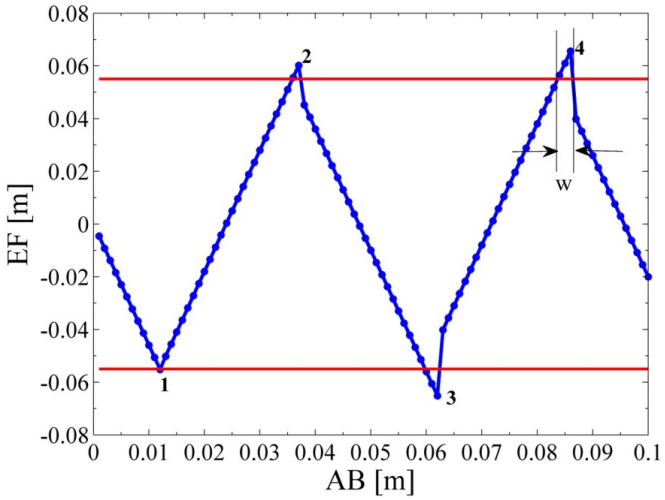

Figure 5. Calculated distances from centre (EF) on the moderator as a function of distance from the monitor (AB) for the guide length of 42.8 m. The red lines mark the height of the moderator. Each blue symbol denotes the originating neutron location. Each peak numbered with 1, 2, 3 and 4 corresponds to the labelled artefacts in figure 3d. The artefact width is denoted by w.

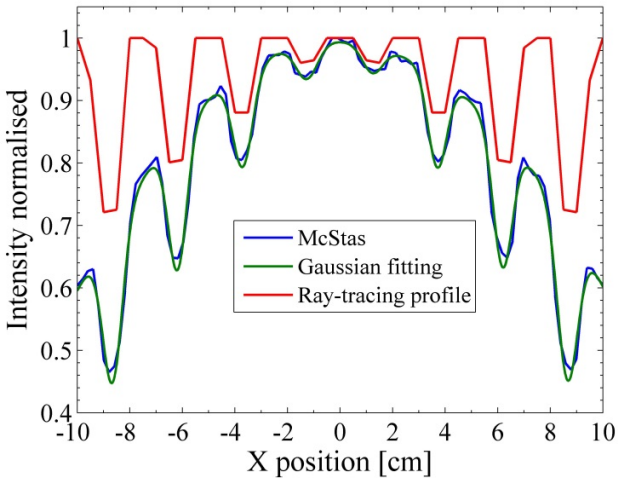

Figure 6. McStas profile plot of the PSD (blue) fitted with Gaussian curve (green). The red plot is the two-dimensional profile calculated based on the ray-tracing code for a pinhole diameter 10 mm and guide length of 42.8 m.

which are deeper towards the edge of the PSD. This is because the neutron trajectories with the higher reflection angles 'see' more of the areas around the moderator which do not emit neutrons.

Having identified the cause of the artefacts as being due to the PSD 'seeing' areas outside of the moderator suggests possibility of reducing them: (i) by making the moderator larger than the neutron guide cross section; (ii) by reducing the distance between moderator and the guide entrance or, (iii) by reducing the guide cross section compared to the moderator size, all of which reduce the effect of under-illumination of the guide entry. While the first two approaches were precluded due to the engineering constraints, the third, to reduce the guide cross section, was considered feasible.

proofs JINST_003P_0713

Table 2. Positions (from centre), heights, areas and widths of artefacts for D=5 mm and D=10 mm by Gaussian fitting of the McStas simulated dips in the distribution (figure 6, green curve). Positions and widths are compared to the predicted parameters from the ray-tracing code taken from figure 5. The error bar for heights can be determined from the errors of area and FWHM of the Gaussian.

Pinhole diameter [mm]	Peak index	Position [cm]		Height [counts/s]	Area [counts/s]	Widths [cm]	
		Gaussian	Ray-tracing			FWHM (Gaussian)	Ray-tracing (w)
5 mm	1	1.29(7)	1.20(1)	3751.28	1568(603)	0.39(16)	0.08(1)
	2	3.83(2)	3.71(1)	10228.14	4447(630)	0.41(7)	0.20(1)
	3	6.36(2)	6.20(1)	15169.65	6918(633)	0.43(4)	0.28(1)
	4	8.91(1)	8.62(1)	18637.69	9481(674)	0.48(3)	0.30(1)
10 mm	1	1.22(10)	1.20(1)	6971.51	7323(1640)	0.98(25)	0.08(1)
	2	3.69(3)	3.71(1)	21904.87	19372(1504)	0.83(7)	0.20(1)
	3	6.17(2)	6.20(1)	31062.65	27284(1499)	0.82(5)	0.28(1)
	4	8.65(2)	8.62(1)	37131.85	34613(1544)	0.87(4)	0.30(1)

Guides with different cross sections, smaller than the area of the moderator face, and same length (i.e. 42.8 m), were investigated using the McStas IMAT imaging model in order to see the reducing effect of the artefacts (figure 7) and keeping a higher neutron flux. Figure 8 shows integrated neutron flux values normalised to their maximum, versus the side length of the neutron guide. For a guide size up to 8.6 cm the neutron flux increases. For a PSD of $20\times20\,\mathrm{cm}^2$ at the monitor position and with a pinhole with diameter of 10 mm, the averaged neutron intensity decreases for guide sizes larger than 8.6 cm. For the diffraction case, the pinhole is removed and the intensity on a PSD of $1\times1\,\mathrm{cm}^2$ at the sample position follows a similar curve of rising and decreasing intensity, however with the maximum flux shifted towards higher guide sizes compared to the imaging case. Due to engineering constraints on the IMAT port on TS-2 the maximum guide cross section is $95\times95\,\mathrm{mm}^2$ which was adopted and considered as an acceptable compromise between imaging and diffraction requirements. With this guide size it is observed that the imaging and diffraction modes lose 2% and 8% respectively of the maximal flux for the respective mode.

It is well known that artefacts are produced by other imperfections in the neutron guide system apart from the above considered under-illumination. Gaps in the neutron guide, lateral and angular misalignments of sections of the guide will lead to artefacts which add to the ones due to the finite size of the moderator.

2.3.2 IMAT instrument design summary

Taking into account the above results on the causes of artefacts in the beam at the detector position, and other technical and engineering constraints, the following IMAT instrument design was adopted.

IMAT will have a straight, square supermirror guide which will start as close as possible to the moderator centre at 1.7 m and will transport the neutrons to the pinhole selector position. The best coating of the guide was determined with regards to integrated intensity maximisation at the

proofs JINST_003P_0713

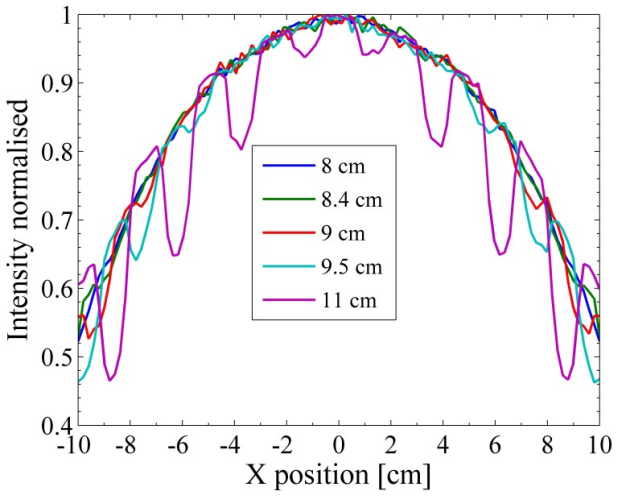

Figure 7. McStas profile plot of the PSD for different guide cross section, guide length 42.8 m and pinhole diameter 10 mm. For the guide cross section with the same size as the moderator, $11\times11\,\mathrm{cm}^2$ the artefacts are visible. By decreasing the guide cross section the artefacts are reduced.

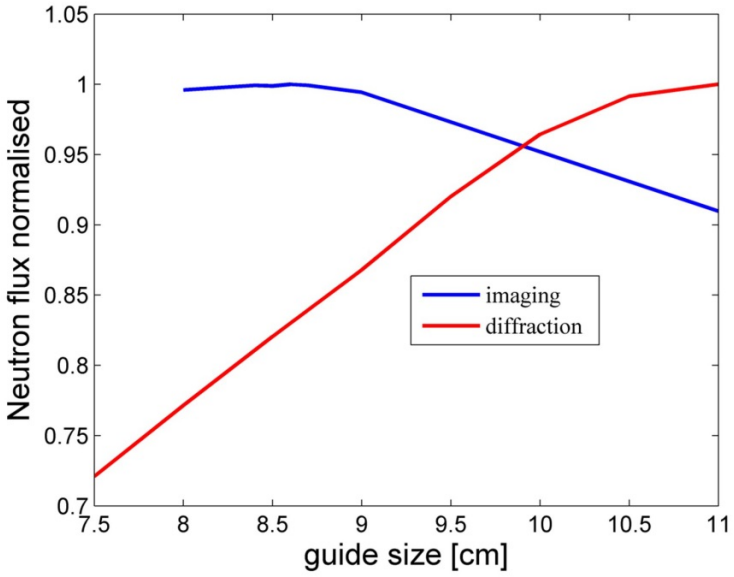

Figure 8. Neutron flux calculated on the sample position as function of side length of the neutron guide in both modes, imaging and diffraction, for a guide length 42.8 m and an m-coating of 3 and a pinhole diameter of 10 mm.

sample position, cut-off at short wavelength, and costs, yielding m=3. The total length of the neutron guide system is 44 m, thereby providing a long flight path to achieve the time resolution required for energy selective imaging and diffraction experiments. The guide will have a cross section of $100\times100\,\mathrm{mm}^2$ in the 2 m shutter section and a cross section of $95\times95\,\mathrm{mm}^2$ throughout the remainder of the guide [1]. From the pinhole selector the beam passes through evacuated tubes to the sample area. The sample position corresponds to a flight path of 56 m from the moderator

proofs JINST_003P_0713

Table 3. Average and peak neutron fluxes on the PSD for different pinhole sizes for two wavelength bands.

Wavelength band [Å]	Pinhole diameter [mm]	L/D	Divergence [°]	Average flux [n/cm^2/s] $\times 10^7$	Peak flux [n/cm^2/s] $\times 10^7$
0.7–7	5	2000	0.029	0.069	0.15
	10	1000	0.057	0.278	0.514
	20	500	0.115	1.12	1.94
	40	250	0.229	4.44	7.15
	80	125	0.458	17.2	26.9
2–14	5	2000	0.029	0.068	0.15
	10	1000	0.057	0.27	0.463
	20	500	0.115	1.12	1.66
	40	250	0.229	4.44	6.43
	80	125	0.458	17.2	24.3

centre and is positioned 10 m after the pinhole, providing a large area for the installation of imaging cameras in transmission and diffraction detectors (table 1).

2.3.3 Neutron flux distributions for varying pinhole sizes

Beam characteristics of a more refined McStas instrument model were simulated based on the instrument description 2.3.2 and table 1. 10^{10} neutrons were generated in the wavelength band 0.7–7 Å and 2–14 Å. In order to simulate the neutron flux at the sample position and study the white-beam intensity distributions on the imaging screen, McStas simulations were performed for different pinhole diameters of 80, 40, 20, 10 and 5 mm. Figure 9 shows that as the pinhole size is reduced the intensity distributions on the imaging screen become more inhomogeneous, exhibiting a clearer pattern of artefacts. For the smaller L/D (e.g. pinhole diameter of 80 mm) these artefacts are assumed to be present but washed-out due to the increased pinhole size allowing a range of neutron trajectories to reach each point on the detector, some of which will arrive from proper reflecting parts of the neutron guide. For a better visualization of the artefacts, profile plots of the monitor counts were considered, by averaging over 20 horizontal lines at the centre of the PSD and by plotting these as a function of horizontal position parameter. In the absence of gravity the neutron intensity distribution is symmetrical, so we may equivalently plot profiles on horizontal or vertical sections.

The highest neutron flux of about 10^8 neutrons/cm^2/s is obtained for the largest pinhole with L/D=125. By decreasing the pinhole size to 0.01 m (L/D = 1000) the neutron flux is down to 3×10^6 neutrons/cm^2/s. Table 3 summarizes the anticipated neutron fluxes for varying L/D values and for two broad 'white-beam' wavelength bands of 0.7–7 Å and 2–14 Å. For each pinhole size the average neutron flux is obtained by dividing the total neutron intensity output of the PSD by the monitor area (400 cm^2) and the peak flux by dividing the maximum neutron intensity by the individual pixel size (0.04 cm^2). Table 3 also lists, for each pinhole diameter, the beam divergence θ based on the standard formula $\theta = \tan^{-1}\frac{D}{L}$, for given L/D values. It should be mentioned that the agreement of average flux values obtained for the two wavelength bands is simply coincidental.

proofs JINST_003P_0713

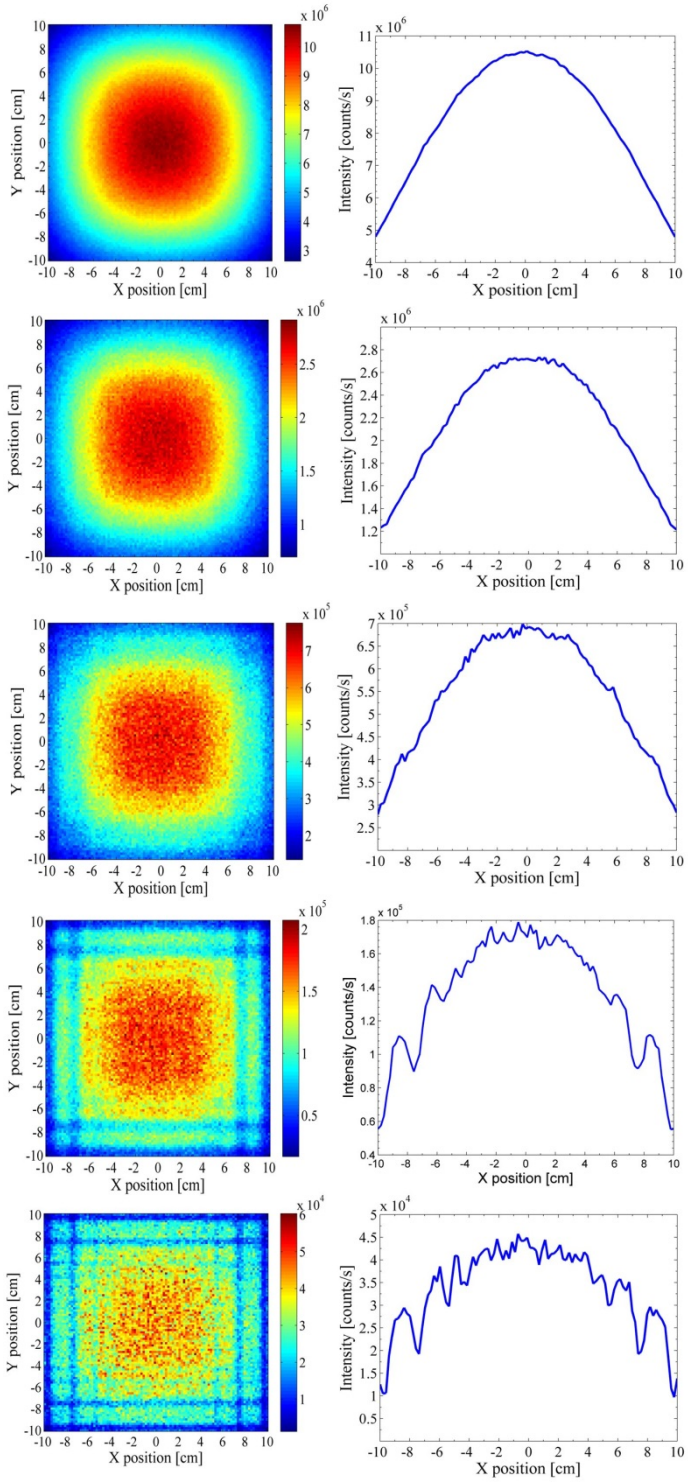

Figure 9. Intensity distributions on the imaging detector for five different apertures with diameter of 80, 40, 20, 10 and 5 mm as a function of position on a $20\times20\,\mathrm{cm}^2$ monitor screen (left column). The right hand column of figures shows the horizontal intensity profile through the centre of the screen (y=0 mm). For each profile, 20 horizontal lines from the PSD centre were averaged in order to improve the statistics.

proofs JINST_003P_0713

Table 4. Average and peak neutron flux on the PSD depending on the pinhole size for different wavelength bands and two pinhole diameters.

Wavelength band [Å]	Pinhole diameter 20 mm		Pinhole diameter 80 mm	
	Average flux [n/cm^2/s] $\times 10^6$	Peak flux [n/cm^2/s] $\times 10^6$	Average flux [n/cm^2/s] $\times 10^6$	Peak flux [n/cm^2/s] $\times 10^6$
1–2	0.81	2.4	12.5	34
3–4	3.3	4.86	51	72
6–7	0.64	0.82	10.1	12
13–14	0.022	0.027	0.34	0.41

2.4 Spatial distribution of intensities for energy selective imaging

IMAT will take advantage of the pulsed source for energy discrimination. The energy-resolved imaging mode will be based on the time-of-flight method and will measure 2D radiographies as a function of wavelength by synchronising the image acquisition with the time structure of the source.

Wavelength-dependent flux and intensity profiles at the monitor position were investigated by selecting four different narrow wavelength bands: 1–2 Å, 3–4 Å, 6–7 Å and 13–14 Å for two pinhole diameters of 0.02 m and 0.08 m. Integrated intensities were obtained by summing all lines of the PSD output, which were then normalized. The intensity profile plots as function of monitor position are shown in figure 10. Table 4 lists the average and peak fluxes for the IMAT beam at 56 m per Å bandwidth. For the smaller pinhole, artefacts are more pronounced for the longer wavelengths towards the edge of the PSD compared to a smoother profile for the short wavelengths. For the larger pinhole the intensity profiles are smoother since the artefacts are washed out. For both pinholes, neutrons with shorter wavelengths are more concentrated in the PSD centre compared to the longer wavelength neutrons which exhibit a flatter distribution, hence potentially providing a larger field of view at these wavelengths. This wavelength-dependent field of view is due to the fact that the longer wavelength neutrons can be reflected through a wider range of angles within the guide and have a higher probability to arrive at the edge of the PSD (since the critical angle, below which neutrons will be reflected, increases with wavelength).

2.5 Spectral distribution across the beam at the sample position

Whereas radiography imaging instruments that do employ a neutron guide have a uniform wavelength distributions across the beam, the wavelength distributions at the IMAT sample position is expected to be non-uniform [4]. In order to further analyse this aspect six small lambda monitors of dimensions $1 \times 2\,\mathrm{cm}^2$ were positioned across the beam at different positions on the camera as indicated in figure 11a.

The first lambda monitor is placed in the centre of the beam followed in the x direction by the other five monitors. The centre of the sixth lambda monitor is at 0.1 m on the x axis (i.e. on the edge of the PSD).

As shown in figure 11b the neutron intensities decrease from the centre of the beam towards the edge (see also figure 9) while the spectrum shifts towards 'colder' neutrons. The shape of the inten-

proofs JINST_003P_0713

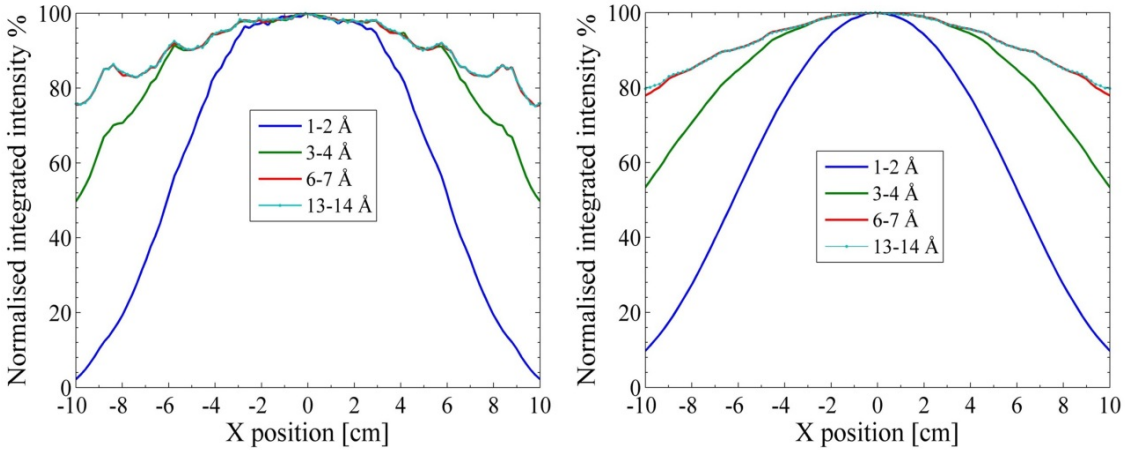

Figure 10. Profile plots of the integrated neutron intensity distributions on the monitor position for different wavelength bands and pinholes of diameter=0.02 m (left) and diameter=0.08 m (right).

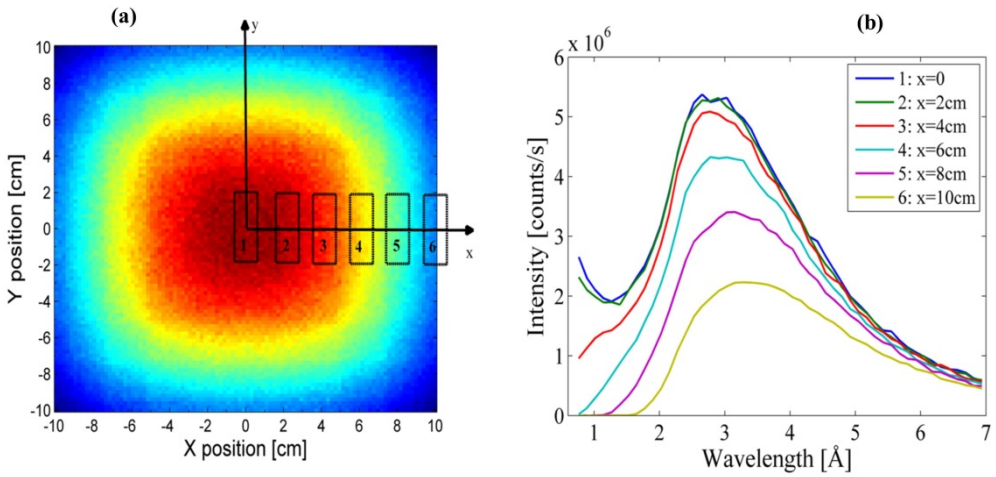

Figure 11. (a) Lambda-monitors (numbered from 1 to 6) are placed in the x-direction across the beam at the monitor position. (b) Intensity as a function of wavelength for each lambda-monitor for wavelength band 0.7–7 Å.

sity distribution in the centre resembles the neutron spectrum leaving the moderator including both shorter and longer wavelengths, i.e. including a proportion of neutrons that have passed straight through the guide without reflection. Moving across the beam to position 6 the short wavelength fraction drops off and the long wavelengths contribute even more to the spectrum, thus shifting the maximum of the spectrum to longer wavelengths as we move to the edge of the monitor.

2.6 Beam divergence across the beam at the sample position

The image quality with regards to spatial resolution depends crucially on the beam divergence, i.e. a larger divergence implies more blurring. The divergence of an imaging beamline is typically controlled by the use of an aperture D at a distance L from the detector, yielding the aspect ratio

proofs JINST_003P_0713

L/D as given above. For large pinholes or for imaging without a pinhole the divergence is also affected by the source divergence or divergence of the neutrons at the exit of a neutron guide. For an imaging instrument on a straight neutron guide where no additional pinhole is used, the beam divergence is defined by the angle θ_c of total reflection of neutrons Moreover, the divergence is constant within the cross section of the guide. In that case the critical angle θ_c is proportional to the neutron wavelength: $\theta_c = 0.1^{\circ} \times \lambda \times \mathrm{m}$ [24, 25]. Hence, if no pinhole is used the beam divergence depends on the wavelength and an effective L/D ratio determines the quality of the projection. For a guide-pinhole system as used for IMAT the divergence was calculated using McStas. The standard divergence/wavelength monitor from McStas calculates the divergence as the angle between the neutron trajectory and the horizontal axis. In fact the divergence at a point is generally the maximum angle between rays passing through that point. Therefore, in order to calculate the correct divergence, the divergence/wavelength monitor from McStas required a minor modification. Small, $1 \times 2\,\mathrm{cm}^2$, modified divergence/wavelength monitors with 50 channels each were positioned as for the lambda monitors shown in figure 11a. These monitors have been made as small as possible, as the ideal was to measure divergence at a point but they needed to be big enough so that each one obtained reasonable statistics. The output of the divergence/wavelength monitor is a distribution of neutron intensity as a function of both divergence and wavelength. Figure 12 shows the results for a pinhole diameter of 40 mm. Figure 12g and h displays the wavelength-integrated profiles which show that the angular ranges are from 0.14° to 0.14° for all positions of the divergence/wavelength monitors. Hence, the maximum beam divergence is approximately 0.28°. The intensity plots exhibit noise due to low counting statistics or larger dips in the profile which correspond to aforementioned artefacts.

The theoretical maximal divergence of a neutron going through the pinhole and arriving on the monitor placed at 10 m after the pinhole could be approximated through the general equation $\theta = \tan^{-1} \frac{D}{L}$ which is independent of the neutron position on the monitor, neglecting the influence of the neutron guide divergence. For a pinhole diameter of 40 mm this value is 0.23° (table 3) which is comparable to the values of 0.28° determined by the modified divergence/wavelength monitor from McStas (figure 12) which include the guide-divergence component.

3 Neutron imaging performance on IMAT

The beam characteristics presented in section 2, i.e. the presence of artefacts and spatial and spectral inhomogeneities, pose challenges for performing imaging experiments on IMAT. The standard method for eliminating beam and detector inhomogeneities from radiographies is the application of a flat field correction. More precisely, by recording the transmitted neutron beam through the sample and the open beam intensity, (without the sample) and dividing the former by the latter, the beam inhomogeneities can be removed. In principle this approach should remove the inhomogeneities (i.e. the artefacts) in the IMAT beam, however it has been observed that other effects, for example the beam profile changing with time, in reactor sources, can make the flat-fielding procedure less effective. One method of reducing problems caused by beam artefacts is to add a graphite diffuser to the beamline [26]. It has been observed that such diffuser filters work well, but at the cost of reducing the neutron intensity at the sample position.

proofs JINST_003P_0713

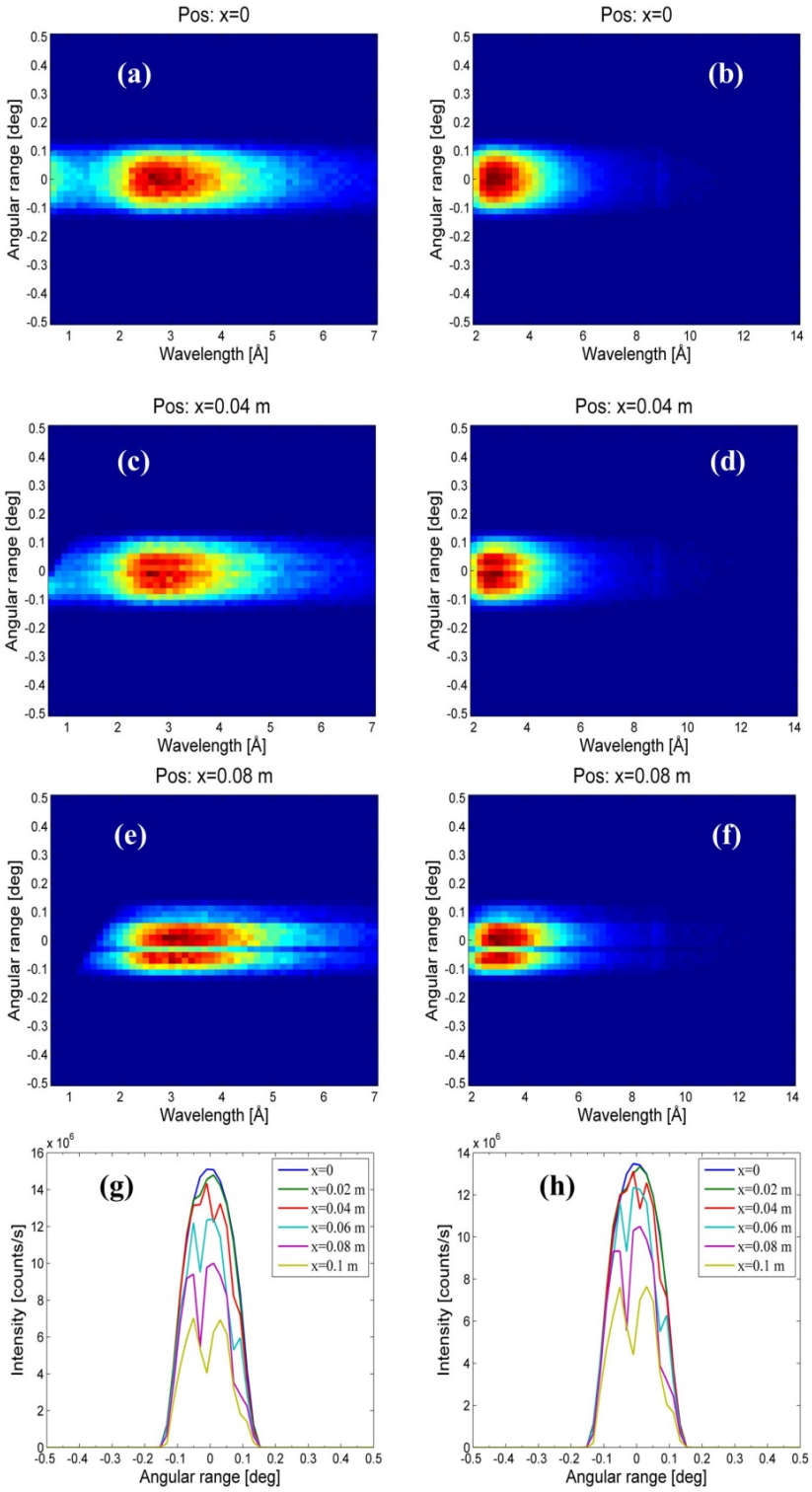

Figure 12. Neutron intensity distribution as function of both divergence and wavelength for position x=0 (a,b), x=0.04 m (c,d) and x=0.08 m (e,f). The pinhole diameter is 40 mm. For white beam imaging the maximum divergence is 0.28° for both bandwidths 0.7–7 Å and 2–14 Å (g,h).

proofs JINST_003P_0713

However, the above flat fielding procedure, which generally uses a white beam, is based on the assumption of linear attenuation, which may not be a good approximation for the case where wavelength dependent attenuation occurs. The use of simple flat fielding in conditions where the assumption of linear attenuation fails results in the phenomenon of beam hardening. In the case of a mono-energetic beam, the Lambert-Beer law $I = I_0 e^{-\mu l}$ is defined as a linear relationship between the proportion of radiation absorbed and the path length through the material. In the case of a polychromatic beam this assertion is not valid because different wavelengths are absorbed differently. Generally, the beam hardening effect is well known in the context of X-ray imaging and describes the fact that low energy X-rays are more easily attenuated than higher energy X-rays [27].

In order to investigate the implications of beam hardening for imaging on IMAT, a theoretical model for studying of the variations of attenuation coefficients owing to the wavelength distribution is presented here. The results from McStas simulations have been combined with a simple model as follows: 10^{10} neutrons were generated in two narrow wavelength bands 3.7–3.9 Å and 4.2–4.4 Å and the corresponding intensity curves I_{01} and I_{02} (figure 13b, blue and green curve, respectively) were extracted from a PSD at the sample position. Attenuation coefficients of $\mu_1 = 0.5\text{cm}^{-1}$ and $\mu_2 = 1.6\text{cm}^{-1}$ were arbitrarily assigned to each beam respectively. A tapered sample with thickness varying from 1 mm up to 1.004 cm was modelled (figure 13a). Given the sample thickness, attenuation coefficients for each selected wavelength bands and the open beam intensities, the intensity profiles of the beam after attenuation due to the sample (I_1, I_2) were obtained by applying the Lambert-Beer law (figure 13c). The two wavelength bands selected could be considered together as a 'white' beam (or so-called, 'total open beam' as the red curve in figure 13b) and the effective attenuation coefficient $(\tilde{\mu})$ (figure 13d) could be derived from equation $\tilde{\mu} = -\frac{1}{l} \ln\left(\frac{I_1+I_2}{I_{01}+I_{02}}\right)$.

Comparing the effective attenuation coefficient calculated from the white-beam approach with the attenuation coefficients defined for two narrow wavelength bands one can say that the effect of the beam hardening is visible for white-beam situation for IMAT instrument in a sample of non-uniform thickness.

The spectral inhomogeneities introduced in section 2.5 pose a similar challenge to the beam hardening in terms of the determination of attenuation coefficients, although they are not to be confused. In the previous simulation of beam hardening the spectral inhomogeneity from PSD centre to edge was ignored for this reason. In the following the beam inhomogeneity and its effect on the attenuation maps are investigated. Four different materials with varying absorption and scattering cross sections were considered. Table 5 contains the scattering and absorption cross sections, averaged and weighted attenuation coefficients as function of monitor position. Figure 14 shows calculated attenuation coefficient for these four materials using the NXS program [28].

The average attenuation coefficient was obtained by averaging over the wavelength range 0.7–7 Å. An intensity weighted attenuation coefficient for each PSD position was calculated based on the formula, $\mu_w = \frac{\sum \mu_i I_i}{\sum I_i}$, where μ_i is the attenuation coefficient for each wavelength λ_i and I_i is the corresponding intensity curve as displayed in figure 11

Figure 15a illustrates that the attenuation coefficients vary as function of monitor position in the white-beam selection. For a better visualization of the relative variation of the attenuation coefficients, the percentage difference of the attenuation coefficient from the central monitor position is plotted in figure 15b. A strong absorbing material, such as Ag, shows a pronounced deviation

proofs JINST_003P_0713

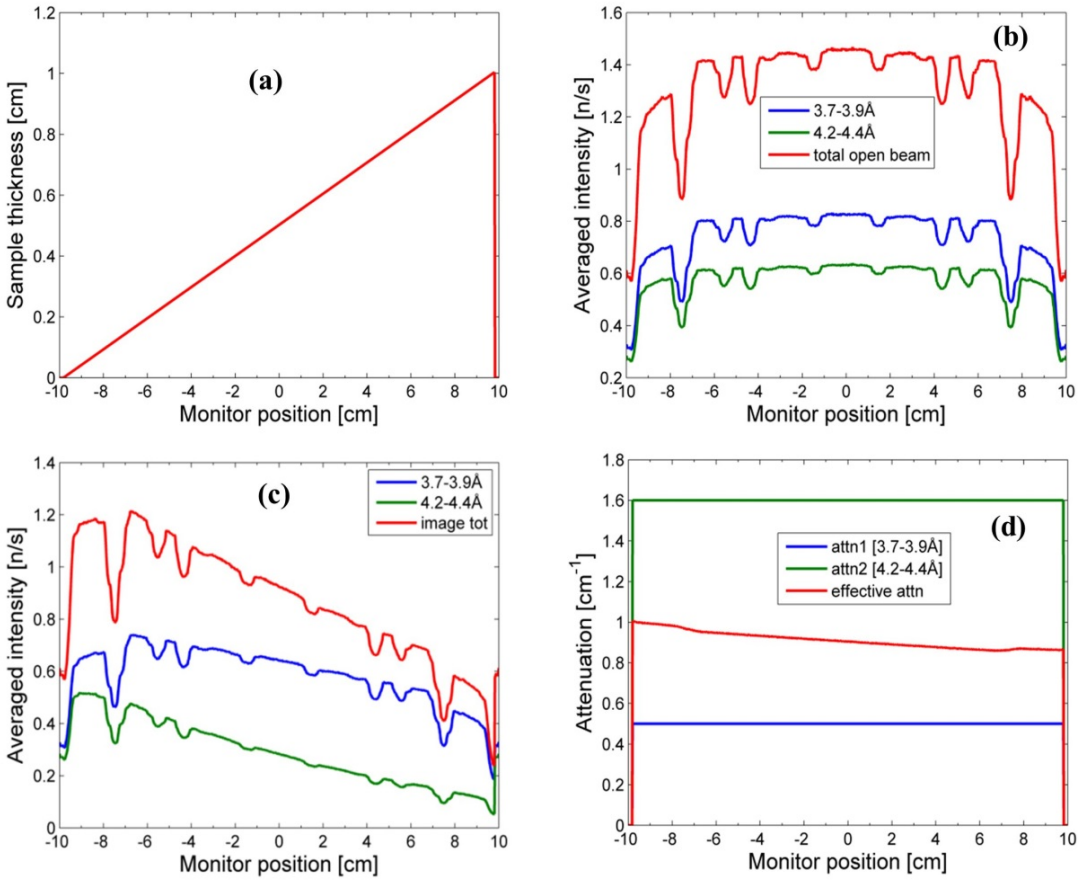

Figure 13. (a) Tapered sample with base of about 20 cm and thickness from 1 mm to 1.004 cm. (b) Open beam profiles for two wavelength bands selected and the "white-beam" profile; (c) Calculated beam profiles using sample thickness, open beam intensities and attenuation coefficients. (d) The attenuation coefficients μ_1 (blue curve), μ (green curve) and the effective attenuation from the "white-beam" case (red curve).

(figure 15b) of up to 20% from centre to edge of the PSD. For weaker absorbers deviations remain within 5%. Figure 15c and d) displays the attenuation curves for the case of a narrower wavelength band of 3–4 Å. The variation of the attenuation coefficients, for the narrow wavelength band of 3–4 Å, from camera centre to edge is less pronounced, less than 1.5% at the edge of the PSD of $20\times20\,\mathrm{cm}^2$.

In the McStas model, one can only choose a monochromatic beam, having a single wavelength, at the expense of impracticably long computing times. On IMAT, small wavelength bins or narrow bands can be selected using the time-of-flight approach, hence giving the opportunity to measure materials with small variations of attenuation coefficients across the field-of-view if necessary, and thus reducing the effect of spectral inhomogeneities on the radiographies. In the same way, i.e. by energy-selective imaging, effects of beam hardening can be diminished. It should be noted however that data acquisition times for narrow band widths have to be increased to achieve the same statistical precision of results. For example, for the 3–4 Å wavelength range and an aperture size of 20 mm, the neutron flux is reduced by a factor of three compared to the white beam measurement, resulting in three-fold longer counting times (tables 3, 4).

proofs JINST_003P_0713

Table 5. Averaged and intensity-weighted attenuation coefficients determined as function of monitor position over wavelength band 0.7–7 Å.

Material	Scattering (σ_s) [10^{-24} cm^2]	Absorption (σ_a) [10^{-24} cm^2]	Averaged atten ($\bar{\mu}$) [cm^{-1}]	Weighted attenuation as function of monitor position (μ_w) [cm^{-1}]					
				X=0	X=0.02	X=0.04	X=0.06	X=0.08	X=0.1
Fcc Fe	Strong 9.85	Weak 2.56	1.0668	1.1465	1.1476	1.1461	1.1405	1.1232	1.0953
Fcc Al	Weak 3.457	Weak 0.23	0.08584	0.09358	0.09361	0.09363	0.09352	0.0928	0.0913
SiO2	Medium 5.253(1)	Weak 0.171(1)	0.3	0.28422	0.2842	0.28423	0.28431	0.2852	0.2873
Ag	Medium 6.502	Strong 63.3	8.1122	7.0551	7.0620	7.2399	7.58421	8.0132	8.5169

(1) The scattering and absorption cross sections for SiO_2 are calculated based on formula $\sigma = \frac{1\sigma_{Si}+2\sigma_O}{3}$ giving the cross section per atom.

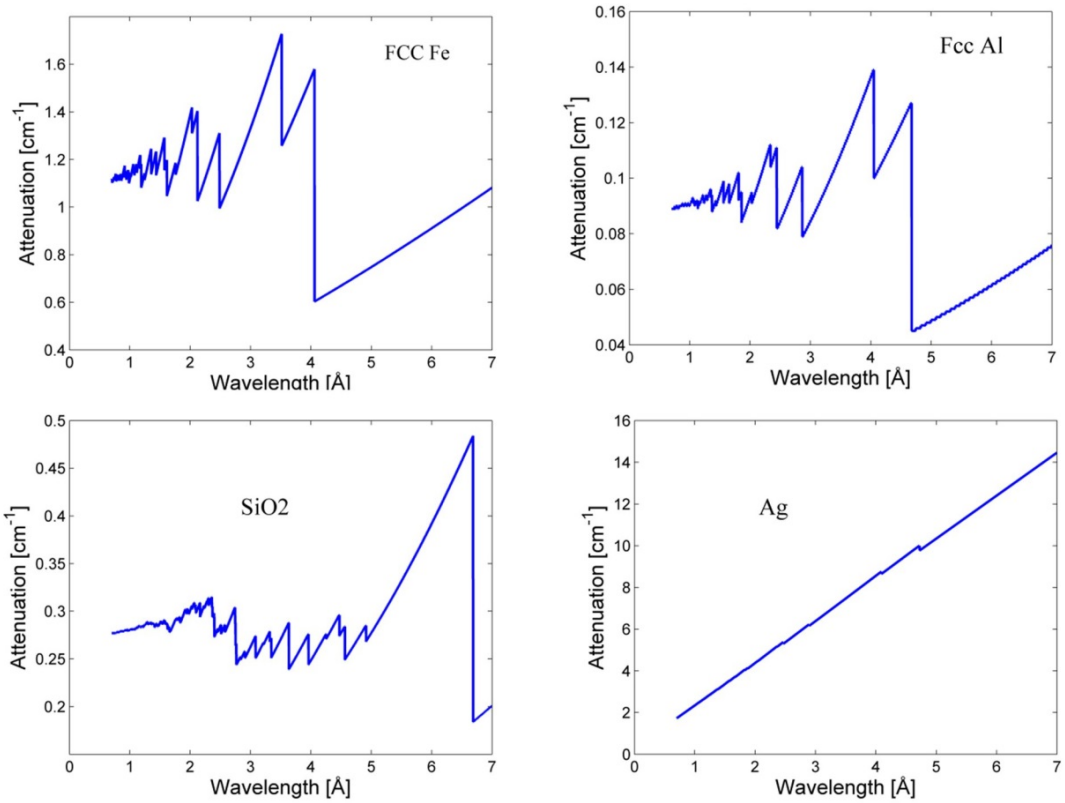

Figure 14. Bragg edge spectra calculated using the NXS program [28].

proofs JINST_003P_0713

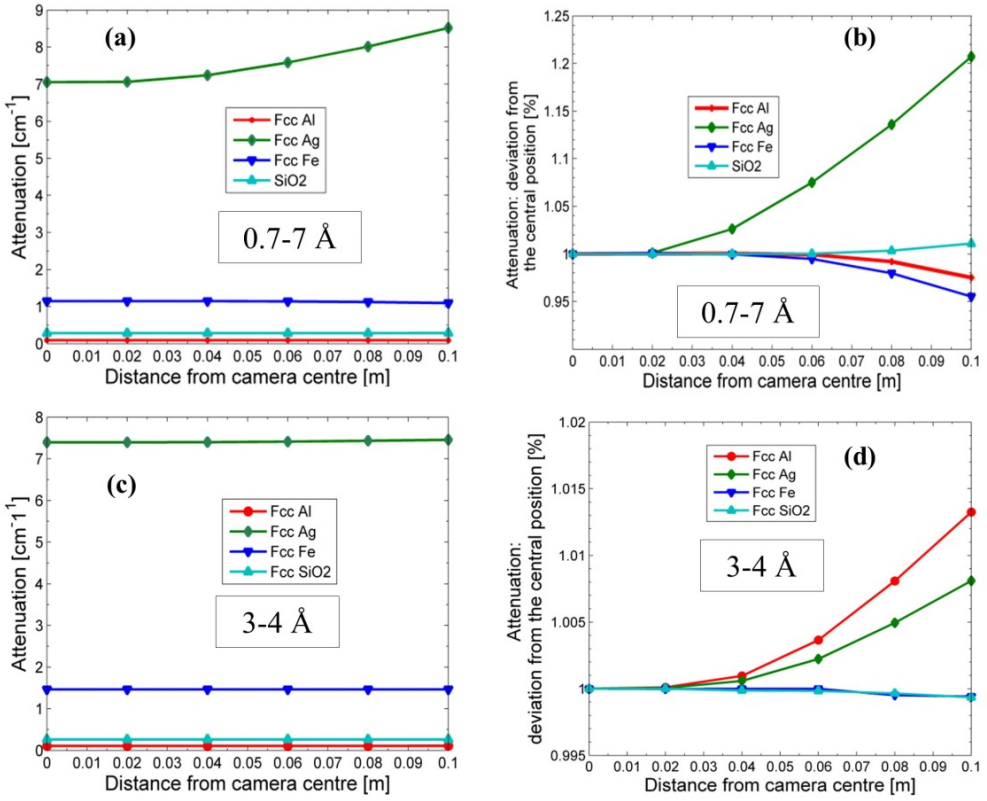

Figure 15. Weighted attenuation coefficients as function of material and monitor position (a,c); deviation of the weighted attenuation coefficient from the camera centre (b,d).

4 Conclusions

The IMAT instrument is presently under construction and is expected to start operation in 2015. The instrument will have a straight square neutron guide with a cross section of $95 \times 95\,\mathrm{mm}^2$ being a suitable compromise between imaging and diffraction requirements. The maximal beam size diameter at the sample position will be approximately 20 cm. The instrument will benefit from a flexible bandwidth selection via choppers and cameras both being synchronised with the pulsed neutron source.

IMAT will have the ability to perform neutron radiography, neutron tomography or energy-selective measurements. The geometrical dimensions of the moderator-guide-pinhole system have been optimized and the resulting performance parameters of the instrument have been determined by Monte Carlo and ray-tracing calculations. The spatial and spectral homogeneity of the beam were characterised, paying particular attenuation to understanding the origin and implications of artefacts within the beam caused by the use of a straight supermirror guide. Spectral inhomogeneities of the beam and beam hardening can be overcome by wavelength-dependent data collection and flat fielding for every wavelength slice.

proofs JINST_003P_0713

Acknowledgments

M.E. Fitzpatrick is supported by the Lloyd's Register Foundation (LRF), a U.K. registered charity and sole shareholder of Lloyds Register Group Ltd that invests in science, engineering and technology for public benefit worldwide.

References

[1] W. Kockelmann et al., *IMAT a new imaging and diffraction instrument at ISIS*, *Physics Procedia* **43** (2013) 100.

[2] Oak Ridge National Laboratory, http://neutrons.ornl.gov/venus/ (2013).

[3] Y. Kiyanagi et al., *Present status of research on pulsed neutron imaging in Japan*, *Physics Procedia* **43** (2013) 92.

[4] N. Kardjilov et al., *Neutron tomography using an elliptic focusing guide*, *J. Appl. Phys.* **108** (2010) 034905.

[5] R. van Langh et al., *New insights into alloy compositions: studying Renaissance bronze statuettes by combined neutron imaging and neutron diffraction techniques*, *J. Anal. At. Spectrom.* **26** (2011) 949.

[6] G. Burca et al., *A new bridge technique for neutron tomography and diffraction experiments*, *Nucl. Instrum. Meth.* **A 651** (2011) 229.

[7] K. Lefmann and K. Nielsen, *McStas a general software package for neutron ray-tracing simulations*, *Neutron news* **10** (1999) 20.

[8] A.A van Well et al., *The average number of reflections in a curved neutron guide*, *Nucl. Instrum. Meth.* **A 309** (1991) 284.

[9] N. Kardjilov et al., *New features in cold neutron radiography and tomography Part II: applied energy-selective neutron radiography and tomography*, *Nucl. Instrum. Meth.* **A 501** (2003) 536.

[10] W. Treimer et al., *Wavelength tunable device for neutron radiography and tomography*, *Appl. Phys. Lett.* **89** (2006) 203504.

[11] M. Tamaki, *Conceptual monochromatic digital neutron radiography using continuous cold neutron beam*, *Nucl. Instrum. Meth.* **A** 542 (2005) 32.

[12] W. Kockelmann et al., *Energy-selective neutron transmission imaging at a pulsed source*, *Nucl. Instrum. Meth.* **A** 578 (2007) 421.

[13] J.R. Santisteban et al., *Engineering applications of Bragg-edge neutron transmission*, *Appl. Phys.* **A 74** (2002) s1433.

[14] J.W.G. Thomason, *Upgrades to ISIS for the New Second Target Station*, *Proc. EPAC08* (2008) 2902 [http://accelconf.web.cern.ch/AccelConf/e08/papers/thxg03.pdf].

[15] G. Salvato et al., *An apparatus for measuring the timing properties of scintillators for neutron imaging*, *Nucl. Instrum. Meth.* **A 621** (2010) 489.

[16] A.S. Tremsin et al., *High resolution photon counting with MCP-Timepix quad parallel readout operating at >1 KHz frame rates*, *IEEE Trans. Nucl. Sci.* **60** (2013) 578.

[17] A. Tremsin et al., *Energy-resolving neutron transmission radiography at the ISIS pulsed spallation source with a high-resolution neutron counting detector*, *IEEE Trans. Nucl. Sci.* **56** (2009) 2931.

proofs JINST_003P_0713

[18] K. Shankland and T. Griffin, *Grid powers up at ISIS*, *Scientific computing world*, Oct/Nov 2005.

[19] K. Shankland et al., *Large-scale distributed computing for accelerated structure solution*, *Z. Kristallogr. Suppl.* **30** (2009) 227.

[20] E. Farhi and P. Willendrup, *Virtual experiments in a nutshell: simulating neutron scattering from materials within instruments with McStas*, *Collection SFN 12* (2011) 303–339.

[21] S.M. Bennington et al., *ISIS target Station II: preliminary target and moderator simulations*, *J. Neutron. Res.* **11** (2003) 93.

[22] D.B. Pelowitz, *MCNPX User's Manual version 2.5.0*, Los Alamos National Laboratory report LA-CP-05–0369 (April 2005).

[23] G. Burca, *Combined neutron imaging and diffraction: instrumentation and experimentation*, Ph.D. Thesis, Milton Keynes, U.K. (2012).

[24] B. Schillinger et al., *3D neutron computed tomography: requirements and applications*, *Physica* **B 276–278** (2000) 59.

[25] N. Kardjilov, *Further developments and applications of radiography and tomography with thermal and cold neutrons*, Ph.D. Thesis, Munchen, Germany (2003).

[26] N. Kardjilov, personal communication (2013).

[27] J.F.Barrett and N. Keat, *Artifacts in CT: Recognition and Avoidance*, *RadioGraphics* **24** (2004) 1679.

[28] M. Boin, *nxs: a program library for neutron cross section*, *J. Appl. Cryst* **45** (2012) 603.

proofs JINST_003P_0713